Advances in Geo-Energy Research

Vol. 13, No. 3, p. 203-217, 2024

Original article

Microfluidic insights into CO_2 sequestration and enhanced oil recovery in laminated shale reservoirs: Post-fracturing interface dynamics and micro-scale mechanisms

Lei Li[1,2,3], Dian Zhang[1,2,3], Yuliang Su[1,3]*, Xue Zhang[1,3], Mingjing Lu[1,3], Hongsheng Wang[4]

[1]*State Key Laboratory of Deep Oil and Gas, China University of Petroleum (East China), Qingdao 266580, P. R. China*

[2]*Sinopec Petroleum Exploration and Production Research Institute, Beijing 102206, P. R. China*

[3]*School of Petroleum Engineering, China University of Petroleum (East China), Qingdao 266580, P. R. China*

[4]*Department of Mining and Mineral Engineering, Virginia Tech, Blacksburg 24061, USA*

Keywords:
CO_2 huff-n-puff
imbibition mechanism
laminated shale
interface instability
multi-scale heterogeneity

Cited as:
Li, L., Zhang, D., Su, Y., Zhang, X., Lu, M., Wang, H. Microfluidic insights into CO_2 sequestration and enhanced oil recovery in laminated shale reservoirs: Post-fracturing interface dynamics and micro-scale mechanisms. Advances in Geo-Energy Research, 2024, 13(3): 203-217.
https://doi.org/10.46690/ager.2024.09.06

Abstract:
Subsequent CO_2 injection can enhance oil recovery and achieve carbon sequestration in shale reservoirs, which is crucial for energy sustainability and environmental protection. However, for continental sedimentary shale oil, the development process must consider the multiscale matrix-fracture structure and the impact of heterogeneous wettability on fluid-solid interactions. Moreover, the mechanisms of CO_2 miscibility and interfacial behavior in post-fracturing reservoirs remain unclear. In this study, a laminated shale micro-model with fracture based on scanning electron microscopy observations was designed, and the process of fracturing fluid flowback and subsequent CO_2 huff-n-puff were simulated. Results showed that forced imbibition primarily affects limestone layers, while spontaneous imbibition affects mudstone layers, contributing 89.3% and 10.7% to the affected area, respectively. The oil recovery mechanism of CO_2 is mainly influenced by pressure, transfer from displacement-carry at low pressure to dissolution-extraction, and eventually to diffusion-extraction in the miscible state. Additionally, before reaching miscibility, Taylor dispersion, Kelvin-Helmholtz instability, Rayleigh-Taylor instability, and Marangoni effects occur at the oil-CO_2 interface, leading to interfacial turbulent instability. Lastly, water huff-n-puff produces membrane and isolated droplet residual oil, while immiscible CO_2 breaks cluster residual oil into columnar residual oil. Miscible CO_2 enhances the recovery of various residual oils, improving oil recovery and facilitating CO_2 storage. This study provides insights for post-fracturing CO_2 huff-n-puff development of continental sedimentary shale oil and CO_2 sequestration, promoting energy utilization and environmental improvement.

1. Introduction

Global shale oil resources are abundant, with a wide distribution and diverse forms of occurrence (Feng et al., 2020). Due to the ultra-low porosity and permeability characteristics and the complex heterogeneity of shale formations (Fang et al., 2019), shale oil production rate is exceedingly slow. Continental shale oil, in particular, presents significant disadvantages compared to marine shale oil. These disadvantages include low kerogen maturity, low pressure coefficients, high clay content, high crude oil viscosity, and insufficient drive energy (Hu et al., 2020; Wang et al., 2022). These characteristics lead to considerable development challenges

Yandy Scientific Press

*Corresponding author.
E-mail address: lei.li@upc.edu.cn (L. Li); dianzhang0414@163.com (D. Zhang); suyuliang@upc.edu.cn (Y. Su); upc_zx@163.com (X. Zhang); lumingjing001@126.com (M. Lu); hongsheng@vt.edu (H. Wang).

Received June 25, 2024; revised July 16, 2024; accepted August 8, 2024; available online August 12, 2024.

and result in poor development performance. Currently, large-scale hydraulic fracturing is commonly used to explore shale oil. However, due to the rapid depletion of oil in fractures and the slow replenishment from the matrix, the high initial recovery rates decline rapidly (Gong et al., 2014), making it difficult to achieve sustainable production in shale reservoirs. Therefore, gas injection after hydraulic fracturing can be employed to enhance oil recovery (Chen et al., 2020; Gao et al., 2021). Greenhouse gases such as carbon dioxide (CO_2), which contribute to global warming, are widely sourced and have numerous effective mechanisms for enhancing oil recovery, including viscosity reduction, swelling, and miscibility (Yang et al., 2024). Furthermore, shale reservoirs contain a large number of nanoscale pores, and many researchers have found that CO_2 has a high adsorption capacity in these reservoirs (Wang et al., 2018; Mohagheghian et al., 2019). Carbon capture, utilization, and storage has become a key technology that is highly prioritized and extensively researched by countries worldwide (Bachu, 2016). Therefore, CO_2 injection presents a dual-benefit strategy for enhancing shale oil recovery while simultaneously sequestering greenhouse gases (Zhang et al., 2020; Ren et al., 2022).

Continental shale oil formations exhibit stratified structures in the vertical direction, with laminar structures being the thickest and most widespread (Zhao et al., 2022). Laminated shale reservoirs can be divided into mudstone layers and limestone layers. The mudstone layers primarily consist of organic matter and clay minerals, with pore sizes ranging from 20 to 200 nm. In contrast, the limestone layers are predominantly composed of brittle minerals, with pore sizes mainly ranging from 20 nm to 10 μm (Zhang et al., 2020). The size of the pores determines the permeability of the reservoir, with laminated shale reservoirs displaying multi-scale characteristics of large pore size spans, low porosity, and low permeability. This results in significant permeability differences between the mudstone and limestone layers, leading to distinct fluid flow properties between the two layers. Moreover, the laminated reservoirs exhibit strong vertical heterogeneity in wettability, causing fluid distribution to be highly discontinuous vertically, which further affects the fluid flow characteristics within the reservoir. Due to the pronounced macroscopic and microscopic heterogeneity, the fluid flow mechanisms within laminated shale are complex, thereby increasing the difficulty of shale oil development (Tan et al., 2017; Sang et al., 2022).

Currently, extensive research has been conducted on the complex flow behavior of shale oil-gas-water multiphase fluids in nano- and microscale spaces (Li et al., 2019a, 2019b; Zeng et al., 2020; Wang et al., 2023; Cai et al., 2024). Laboratory core flow experiments are the most intuitive method for studying fluid flow patterns, yet they are limited by precision and experimental apparatus difficulty. In contrast, microfluidic experimental techniques, owing to their precision, quantification, speed, and visualization advantages, have been widely applied in the field of oil and gas development in recent years (Conn et al., 2014; Sieben et al., 2015; Lifton, 2016). These techniques are used to intuitively explore the flow patterns of oil, gas, and water in fractures and nano- and microscale matrices, as well as the mechanisms for enhancing recovery (Lifton, 2016; Fani et al., 2022). Zhang et al. (2023) designed a microchip containing a main channel and four closed side channels to study the impact of asphaltene precipitation in a single tube on CO_2 sequestration and leakage. Jian et al. (2021) investigated the influence of chip geometry, surfactant type and concentration, injection flow rate, and gas and oil fractional flow on the strength of CO_2 foam using a microfluidic device. Nguyen et al. (2018) studied the mechanism of oil recovery during CO_2 and N_2 flooding processes by simplifying the fracture network structure. Mahdavifar et al. (2023) combined microfluidic technology with Lattice Boltzmann methods to explore the effects of pore geometry, flow rate, and asphaltene concentration on deposition behavior. Wang et al. (2023) designed microfluidic chips with porous medium structures and conducted microfluidic experiments to investigate the regulating ability of nanofluids on the oil/water/solid three-phase interface, as well as the dynamics and migration processes of residual oil.

Despite extensive research on CO_2-enhanced oil recovery, the micro-scale mechanisms in post-fracturing laminated shale reservoirs remain poorly understood. Meanwhile, most microfluidic experiments simplify reservoirs to single tubes or homogeneous porous media models, which alters the fluid flow relative to actual reservoir conditions. Previous studies mainly focused on the impact of injection-production parameters on CO_2 recovery efficiency, without considering the multiscale matrix-fracture structure of post-fracturing shale and the influence of wall surface heterogeneous wettability on fluid-solid interactions. Furthermore, detailed reports on the interfacial microscopic mechanisms during the transition of CO_2 from immiscible to miscible states are currently lacking.

Therefore, this study aims to investigate the micro-scale mechanisms of CO_2 sequestration and enhanced oil recovery in laminated shale reservoirs using a microfluidic approach. The microfluidic chip model containing a combination of matrix and fracture were designed to reflect the multiscale heterogeneity characteristics of laminated shale, which obtained from scanning electron microscopy Then, water and CO_2 huff-n-puff experiments were conducted to simulate the processes of imbibition during fracture fluid flowback and subsequent CO_2 enhanced oil recovery (EOR) within laminated shale. The micro-mechanisms of forced imbibition and spontaneous imbibition, as well as the formation mechanisms of different residual oil states were investgated. The influence of mudstone-limestone alternating laminated shale heterogeneity on fluid-solid interactions and flow behavior was clarified. The micro-mechanisms of CO_2 interaction with oil at different stages and interface instability between miscible fluids were elucidated.

2. Methods and materials

2.1 Microfluidic chip design

The laminated shale is composed of limestone and mudstone. Based on the scanning electron microscopy (SEM) analysis of Shengli Oilfield cores with permeability of 0.0185 md and porosity of 5.64%, the two-dimensional characterization of each mineral structure was obtained by noise reduction and

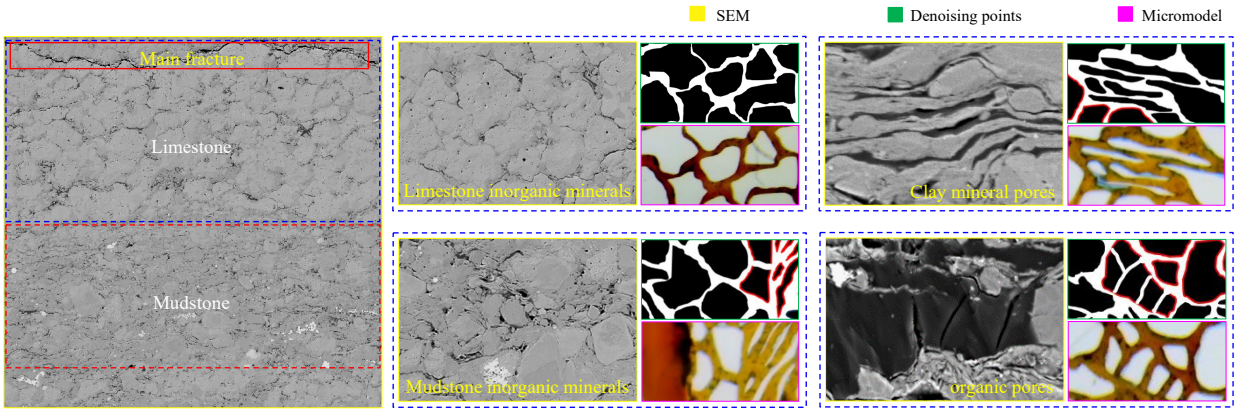

Fig. 1. SEM and laminated shale structure characterization.

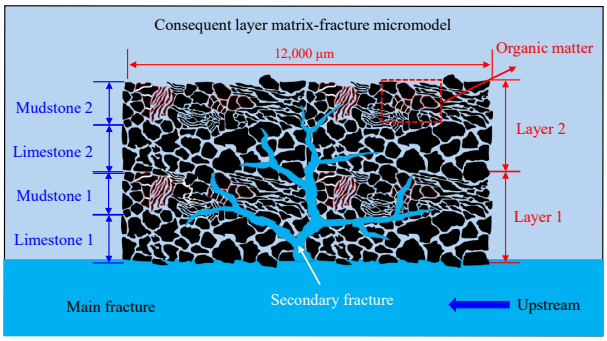

Fig. 2. Laminated shale matrix-fracture micromodel.

simplification of the SEM results after binarization as shown in Fig. 1. The limestone layer is mainly composed of brittle minerals such as quartz, feldspar and calcite. The coordination number is 2-4, and the pore size range is mainly between 20 nm-10 μm. The brittle minerals in the limestone are mostly large particle structures, which are easy to be fractured. Therefore, the fractures are mostly located in the limestone or the mud-lime interlayer. The mudstone layer is mainly composed of organic matter, clay minerals and a small amount of brittle minerals. The coordination number is 1-3, and the pore size range is mainly between 20-200 nm. The organic matter is mainly located inside the clay minerals, while a small amount of brittle mineral particles are scattered in the middle. In addition, the pores in the mudstone layer are mostly consistent with the direction of the lamina, and the longitudinal connectivity is poor.

According to the structural characteristics of laminated shale, the laminated shale models including matrix-fracture combination is obtained as shown in Fig. 2. The microfluidic chip was designed and prepared by combining high frequency hydrofluoric acid etching and thermocompression bonding technology with borosilicate glass (Borofloat33). The model contains a main channel (width × depth = 1,000 μm × 30 μm). Above the main channel is the bedding fracture model obtained by fracturing. The direction of the main fracture is consistent with the direction of the lamina, and the induced fracture extends vertically to the interior of the matrix. In the model, the blue area is the fracture (depth = 30 μm), and the black area is the water-wet area (depth = 15 μm). The red area is the oil-wet area (depth = 15 μm), representing organic matter.

2.2 Microfluidic experimental platform and procedure

The components of the high temperature and high pressure (HTHP) micro-visualization experimental platform is shown in Fig. 3. The platform consists of four parts: Injection system, confining pressure control system, back pressure system and data acquisition system.

The crude oil and CO_2 samples used in this study are consistent with those used by Zhang et al. (2023). The pressure used in the experiments were selected based on typical reservoir conditions and previous studies indicating CO_2 minimum miscibility pressure of 8.5 MPa. The selected soaking and injection pressures cover the supercritical pressure of CO_2, encompassing different stages of CO_2-oil-wall interfacial interactions. This approach facilitates the investigation of microscopic mechanisms related to enhanced oil recovery and interfacial changes. The specific experimental steps are as follows:

1) The microfluidic chip was placed in the HTHP holding chamber for vacuuming, filling the confining pressure water and opening the tracking mode (the confining pressure was higher than the inlet pressure by 1 MPa). The heating device was heated to the preset temperature of 90 °C, and then the vacuum treatment was performed inside the chip.
2) Saturated crude oil inside the chip under atmospheric pressure, and clean the crude oil inside the inlet end pipeline. Then, the outlet end is closed, and the water is injected into the chip through the inlet end to the preset pressure (0.1 MPa in the first cycle, 0.5 MPa in the second cycle, 1 MPa in the third cycle, 1.5 MPa in the fourth cycle, 2 MPa in the fifth cycle) to simulate water forced imbibition.
3) Stand still for 20 minutes to simulate the soaking stage and water spontaneous imbibition. Then, the pressure reduction gradient (0.1 MPa) is controlled by the back pressure pump to reduce the pressure and depressurization development.

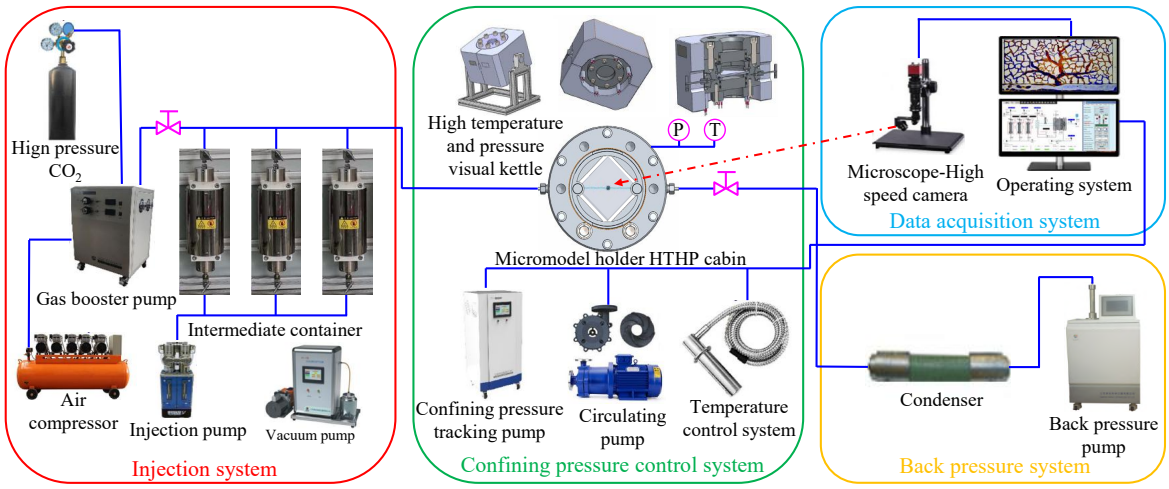

Fig. 3. HTHP microscopic visualization experimental platform.

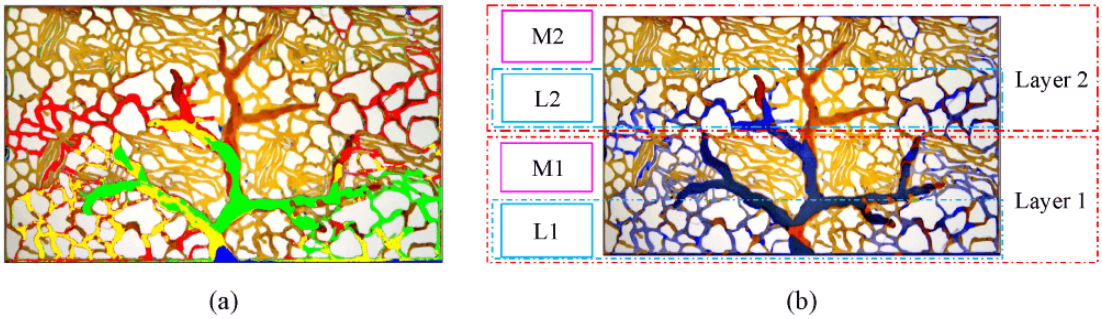

Fig. 4. Water migration trajectory and lamina division: (a) The order of water entering into fracture-matrix and (b) oil-water distribution after water injection pressurization.

4) After repeating five cycles of water huff-n-puff, CO_2 was injected into the chip through the inlet end to make the overall pressure reach 9 MPa.
5) After 20 minutes of soaking, the pressure is reduced to 6.5 MPa (pressure drop gradient 0.1 MPa) through the back pressure pump.
6) Repeat 5 cycles of CO_2 huff-n-puff, and record the experimental data through the data acquisition system.
7) Clean the entire HTHP micro-visualization experimental platform with petroleum ether.

3. Results and discussion

3.1 Fracturing fluid injection and flowback

The water huff-n-puff experiment can simulate the process of fracturing fluid injecting into the matrix through the main fracture and the flowback process of fracturing fluid in the field application. The whole huff-n-puff process into three stages: Pressurization stage, soaking stage and depressurization stage. The pressurization stage corresponds to the process in which the fracturing fluid is injected into and spreads the matrix through the main fracture, and the water in this stage is mainly migrates through forced imbibition. The water in the soaking stage mainly migrates through spontaneous imbibition. The depressurization stage corresponds to the flowback process of fracturing fluid, which belongs to depletion development process.

3.1.1 Microscopic mechanism of imbibition

Due to the increasing injection pressure, water in the pressurized stage mainly undergoes forced imbibition. The pressurization stage can be divided into four steps in the mud-lime interactive laminated shale:

1) Dominated by viscous resistance, water preferentially enters induced fractures with larger pore size.
2) Water into the limestone large aperture area.
3) Due to the influence of local pressure, water converges from the limestone to the fractures, and promotes the exploitation of crude oil.
4) When the pressure of water in the fracture is greater than the viscous resistance entering the small pore of the mudstone layer, the water enters the mudstone layer. Water migration trajectory corresponding to different steps are shown in Fig. 4(a). In order to facilitate the description, the laminated shale matrix was divided into four small laminas (two layers) as shown in Fig. 4(b).

The mechanism of water forced imbibition in the pressurization stage is shown in Fig. 5. The forced imbibition of water is mainly affected by local pressure, and the main forms are columnar flow and membranous flow. Due to the high local pressure difference near the main fracture and low viscous

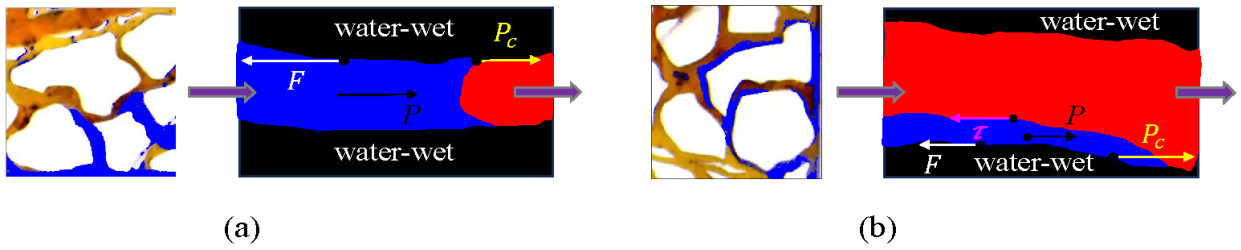

Fig. 5. The mechanism of forced imbibition of water in the pressurization stage: (a) Columnar flow and (b) membrane flow.

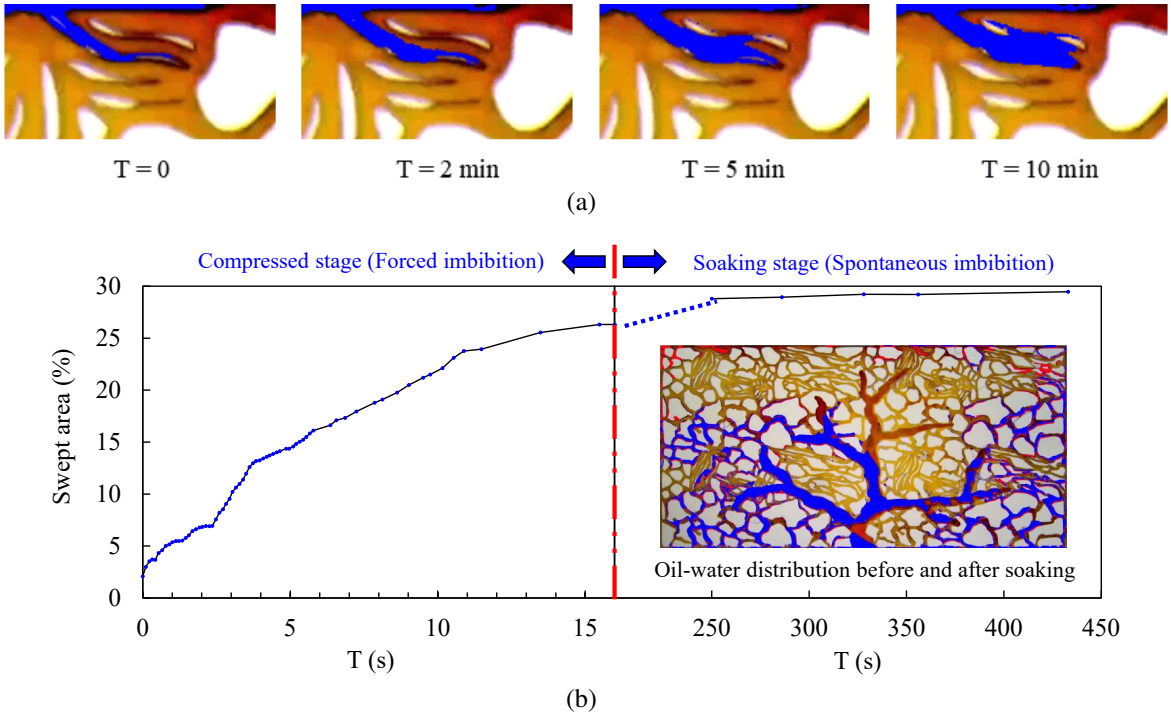

Fig. 6. Membrane spontaneous imbibition and swept area contribution rate: (a) Membrane imbibition and (b) the swept area of the compressed stage and the soaking stage changes with time (The contributions to swept area of forced imbibition to spontaneous imbibition are 89.3% and 10.7%).

resistance in the large pore, the water forms a columnar flow in water-wet wall under the action of pressure gradient P, capillary force P_c and viscous force F, as shown in Fig. 5(a). The driving force generated by the pressure gradient at the limestone lamina is low, and the water forms a membranous flow in water-wet wall under the action of pressure gradient, capillary force, viscous force and viscous shear force, as shown in Fig. 5(b). Due to the decrease of pressure gradient and the obstruction of viscous shear force, the velocity of membranous flow is smaller than that of columnar flow.

3.1.2 Comparison of spontaneous and forced imbibition

The pressure in the soaking stage is kept constant, and the local pressure in each part of the matrix is gradually balanced. Because there is no external force, water enters the pores through spontaneous imbibition as shown in Fig. 6(a). The driving force of spontaneous imbibition is only capillary force, so water forms a membranous flow, and this process (red trajectory in Fig. 6(b) only occurs in the non-oil-wet area of the mudstone lamina with smaller pore size.

Forced imbibition, driven by external forces, results in faster, columnar water flow into the matrix, leaving less residual oil in the pores. In contrast, spontaneous imbibition involves slower, film-like water migration, which is less effective at extracting oil from the pores. In order to explore the effect of each stage of the injected fluid, the first cycle was taken as an example to draw the curve of water sweep area with time, as shown in Fig. 6(b). In Fig. 6(b), the left side is forced imbibition, and the right side is spontaneous imbibition. The swept area of water increases rapidly in the pressurization stage, and the highest is 26.32%. In the soaking stage, the swept area increases slowly, the time scale is large. At the end of the soaking stage, the swept area of water is 29.47%. Therefore, the proportion of water swept area increment in the pressurization stage and the soaking stage can be obtained, that is, the contributions of forced imbibition and spontaneous imbibition are 89.3% and 10.7%, respectively. This shows that oil-water replacement mainly occurs in the fracturing fluid injection period, that is, the pressurization stage.

A total of 5 water huff-n-puff cycles were carried out.

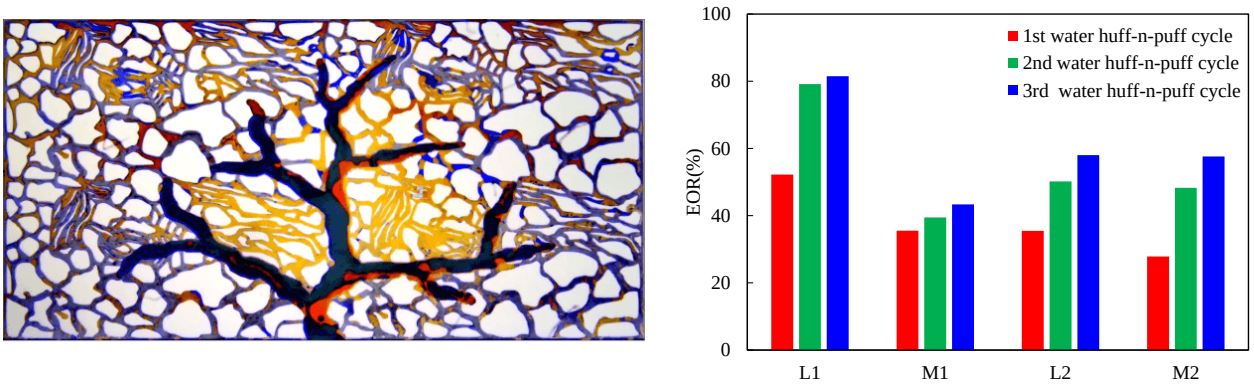

Fig. 7. Oil-water distribution and EOR at the end of water huff-n-puff: (a) Oil-water distribution at the end of water huff-n-puff and (b) EOR.

Since the 4th cycle, there was no change in the water swept area or oil recovery. The oil-water distribution at the end of water huff-n-puff was shown in Fig. 7. The final results of water huff-n-puff are: $EOR_{L1} = 81.5\%$, $EOR_{M1} = 43.35\%$, $EOR_{L2} = 58.01\%$, $EOR_{M2} = 57.6\%$. This proves that forced imbibition can sweep the entire region of limestone lamina 1, and a small part of the mudstone lamina 1 and most of the limestone lamina 2. However, water cannot enter the oil-wet area of the mudstone layer at the intersection of induced fractures, thus forming a dead oil area. In fact, the water even crossed the mudstone lamina 1 and spread to the limestone lamina 2 in a large area. The sweep area of the first cycle is the largest, so in practical applications, the injection pressure and injection time of the fracturing fluid should be increased to increase the sweep area and EOR. These results are consistent with the theoretical research by Cai and Yu (2011) and Deng and King (2019). The advanced part of this study is to validate the dominant roles of capillary and viscous forces through microscopic experiments and compared the sweep efficiency of forced imbibition and spontaneous imbibition in laminated reservoirs, which has not been previously reported.

According to the above research results, the first cycle of forced imbibition is the key mechanism during the injection and flowback processes of fracturing fluid. Therefore, in field fracturing operations, it is advisable to appropriately increase the injection pressure and duration of the fracturing fluid while reducing the number of injection cycles.

3.2 Microscopic mechanism of CO_2 huff-n-puff

In this experiment, CO_2 is injected into the main fracture and start pressurization until the CO_2-oil is completely miscible. The CO_2 condition from low pressure stage to high pressure stage is as follows: Low-pressure CO_2 (0-6 MPa), supercritical CO_2 (6-7.5 MPa), miscible CO_2 (8.5 MPa and higher).

3.2.1 Interaction between CO_2 and oil

The three states of CO_2 have different microscopic interactions with oil, caused by the difference in diffusion rate and solubility. The diffusion rate is mainly affected by pressure. As the pressure increases, the intermolecular distance decreases, the probability of molecular collision increases, and the average free path decreases. These factors increase the diffusion rate. Solubility is related to pressure and oil composition. Solubility increases with the increase of pressure and decreases with the increase of oil molecular weight.

The process of CO_2 pressurization can be divided into five stages:

1) Low pressure stage: The solubility of low-pressure CO_2 is low, and the oil in the middle of the pores can only be extracted by CO_2 displacing-carrying effect, which creates oil membrane on the wall.
2) Oil expansion stage: When CO_2 enters the supercritical state, its solubility and diffusion rate increase significantly, which will lead to the expansion of oil and compress the space occupied by CO_2 in the matrix. Supercritical CO_2 is used to displace light oil by dissolution extraction, and a transition zone containing a large amount of CO_2 is formed at the two-phase contact.
3) Local miscible phase stage: The pressure in the matrix is higher than that in the fracture. The smaller the pore size, the smaller the energy barrier of CO_2-oil. These factors cause CO_2 in the matrix to preferentially miscible with oil.
4) Transition stage: In this stage, light oil diffuses into the transition zone under the local pressure gradient formed by concentration gradient and velocity.
5) Complete miscible stage: When the oil in the transition zone dissolve a lot of CO_2, the CO_2-oil interface disappears and completely miscible.

Because there is no limitation of interfacial tension, the diffusion rate increases sharply, and the miscible CO_2 mainly extracts oil through diffusion-extraction. In the molecular simulation study by Liu et al. (2024), the miscible behavior of CO_2 and crude oil is divided into four stages, similar to our classification of the different stages of CO_2-oil interactions observed in microscale experiments.

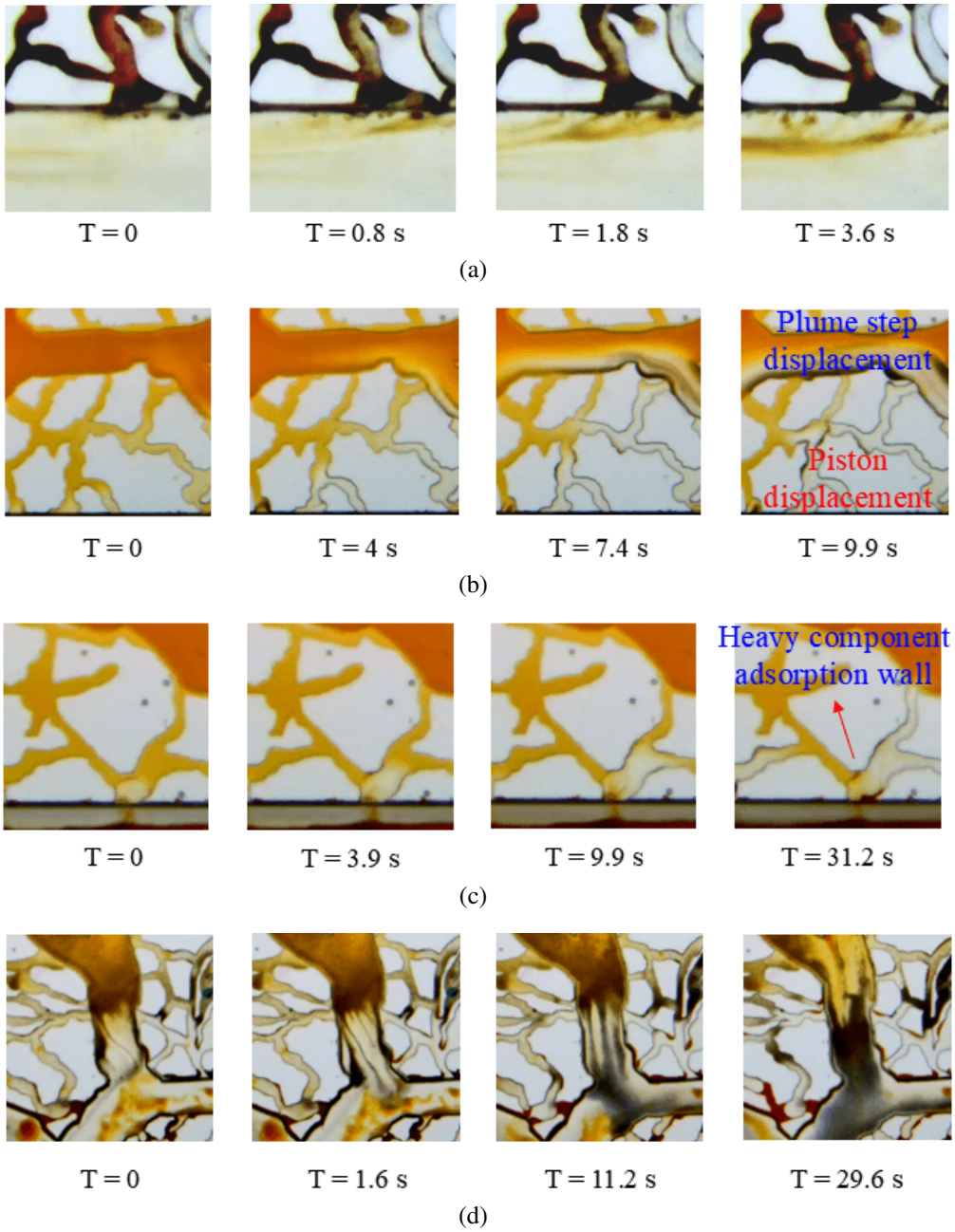

Fig. 8. Microscopic mechanism of miscible CO_2: (a) Advection-diffusion, (b) plume step and piston displacement, (c) CO_2 enters the oil and extracts the light components, and (d) the diffusion of light components into CO_2.

The microscopic mechanism of miscible CO_2 is shown in Fig. 8. CO_2 injection process is dominated by advection-diffusion mechanism, as shown in Fig. 8(a). However, due to the sharp increase of diffusion rate after CO_2-oil miscible, the diffusion between CO_2 and oil is enhanced, and a large amount of light oil is extracted into CO_2 and migrates rapidly in the main fracture. After the light oil is extracted, the heavy oil is adsorbed on the wall to form the migration trajectory shown in the Fig. 8(a). This process is related to the interaction energy between molecules. The interaction energy of CO_2-oil molecule increases with the increase of pressure, while the interaction energy of quartz-oil molecule is just the opposite. Therefore, the increase of CO_2 pressure weakens the adsorption capacity of quartz-oil molecules, so the oil is stripped off the wall. This is also the reason why miscible CO_2 can effectively extract membrane oil and corner oil. For different components of oil, the interaction energy between CO_2 and heavy oil is much smaller than that of light and medium components, while the interaction energy between heavy oil and quartz does not change much. Therefore, the heavy component is difficult to miscible with CO_2, so it is adsorbed on the quartz wall.

The pore structure generates local pressure gradient in fr-

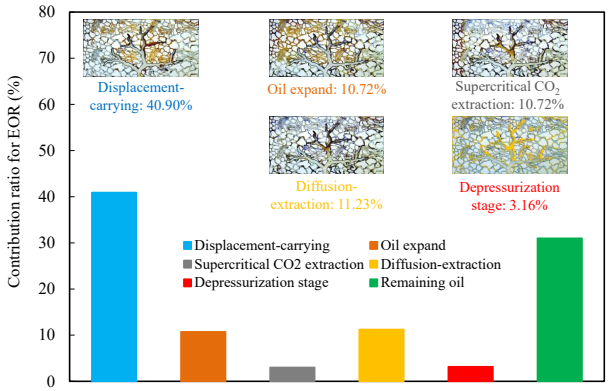

Fig. 9. The proportion of crude oil produced by different CO_2 displacement mechanisms.

actures and matrix, causing plume step displacement in fracture and piston displacement in matrix pores, as shown in Fig. 8(b). The diffusion-extraction process is shown in Figs. 8(c)-8(d). This process can be divided into two types: CO_2 entering oil and oil entering CO_2. The main reason for its formation is the increase of diffusion rate. In Fig. 8(c), CO_2 enters the oil and extracts the light components, resulting in the adsorption of heavy components on the pore wall. In high-pressure conditions, the solubility of light hydrocarbons in CO_2 increases markedly, and the diffusion of light components into CO_2 plays a significant role, as shown in shown in Fig. 8(d). This is because the CO_2 acts as a solvent, reducing the interfacial tension between oil and CO_2, allowing the oil to flow more freely. Moreover, the increased pressure helps to drive CO_2 deeper into the reservoir, enhancing contact with more oil. The combination of these effects, enhanced solubility, reduced viscosity, and improved displacement efficiency, contributes to the overall effectiveness of CO_2 in extracting oil from laminated shale reservoirs.

The proportion of crude oil produced by different CO_2 displacement mechanisms is shown in Fig. 9. Low-pressure CO_2 can drive 40.9% of oil through displacement-carrying, which mainly comes from water-wet macropores in fractures, limestones and mudstones. Supercritical CO_2 dissolves in oil, making oil expand, and 10.72% of oil can be produced, which mainly come from the clay mineral area and oil-wet area in the mudstone lamina. Subsequently, 3% of oil can be extracted by supercritical CO_2 extraction. When CO_2-oil is completely miscible, CO_2 spreads to deeper lamina and extracts 11.23% of oil by diffusion-extraction. In addition, in the depressurization stage, oil production increased by 3.16%. Most of them are heavy oil, which are explored by CO_2 displacement-carrying.

In the miscible state, the factors influencing CO_2-enhanced oil recovery include pressure and pore structure. Pressure affects CO_2 solubility, interaction energy, and molecular diffusion rates, which in turn impact the degree of CO_2-oil miscibility and the efficiency of CO_2-driven oil recovery. Pore structure influences the contact area between CO_2 and crude oil, affecting the mass transfer rate and thus the efficiency of oil recovery. Additionally, pore size alters the energy barrier at the CO_2-oil interface, affecting the level of miscibility. These findings are consistent with the research by Chen et al. (2023). Convective-diffusion primarily depends on the control of displacement pressure gradients and the preferential flow paths through high-permeability zones, while mass transfer is mainly determined by the extent of convective-diffusion and the degree of CO_2-oil miscibility.

3.2.2 Interface instability in miscible process

The most obvious difference between miscible CO_2 and immiscible CO_2 is the existence of the interface. When the supercritical state is pressurized to the miscible state, the migration velocity of CO_2 increases due to the change of compressibility. This will cause uneven rapid mass transfer between CO_2 and oil. The interphase mass transfer will lead to a local concentration gradient, resulting in a random change in interfacial tension, which will eventually lead to unstable ripples and disturbances at the interface. This phenomenon is called interfacial turbulence/interfacial instability, which occurs near the interface. There are four phenomena that cause uneven mass transfer, which together lead to interfacial turbulence, as shown in Fig. 10.

The Taylor dispersion effect (Frankel and Brenner, 1989; Salles et al., 1993) is shown in Fig. 10(a). When CO_2 reaches the supercritical state, a constant injection rate will rapidly pressurize the CO_2 in the main fracture, which accelerates the flow rate of CO_2 in the main fracture. The velocity difference between the main fracture and the induced fracture produces a local pressure gradient from the matrix to the main fracture, which drives the light oil to diffuse to the transition zone. This diffusion is similar to the Poiseuille flow in a single pipe, which can make the composition of oil gradually close to CO_2.

The Kelvin-Helmholtz (K-H) instability in CO_2-oil miscible phase (Funada and Joseph, 2001; Truzzolillo and Cipelletti, 2017) is shown in Fig. 10(b). It is due to the rapid increase of CO_2 pressure, which creates a tangential velocity difference at the two-phase interface, leading to a vortex-like diffusion phenomenon. The fluid velocities of the lower and upper layers are $\boldsymbol{v}_1$ and $\boldsymbol{v}_2$, the density are ρ_1 and ρ_2, and the potential functions are ϕ_1 and ϕ_2. The two-phase interfacial tension is σ. Assuming that the velocity potential function is a monochromatic plane wave in the x direction, the perturbation of the fluid ξ and the velocity potential function ϕ are:

$$\begin{aligned} \xi &= \xi(x,t) = a\mathrm{e}^{ikx-\omega t} \\ \phi_i(x,z,t) &= f_i(z)\mathrm{e}^{i(kx-\omega t)} \end{aligned} \tag{1}$$

where a is the amplitude, e is the natural constant, i is the period number, k is the wave number, ω is the angular frequency, x and z are the spatial coordinates, t is the time, f_i is the function.

The initial velocity of the two-layer fluid is U_1 and U_2, and the velocity of the two-layer fluid is:

$$\boldsymbol{v}_i = \left(U_i + \frac{\partial \phi_i}{\partial x}, \frac{\partial \phi_i}{\partial z}\right) \tag{2}$$

Assuming that the fluid has no initial velocity, the fluid velocity is zero at infinity, and the velocity of the interface disturbance is vertical to the interface. Therefore, the boundary conditions of the model are:

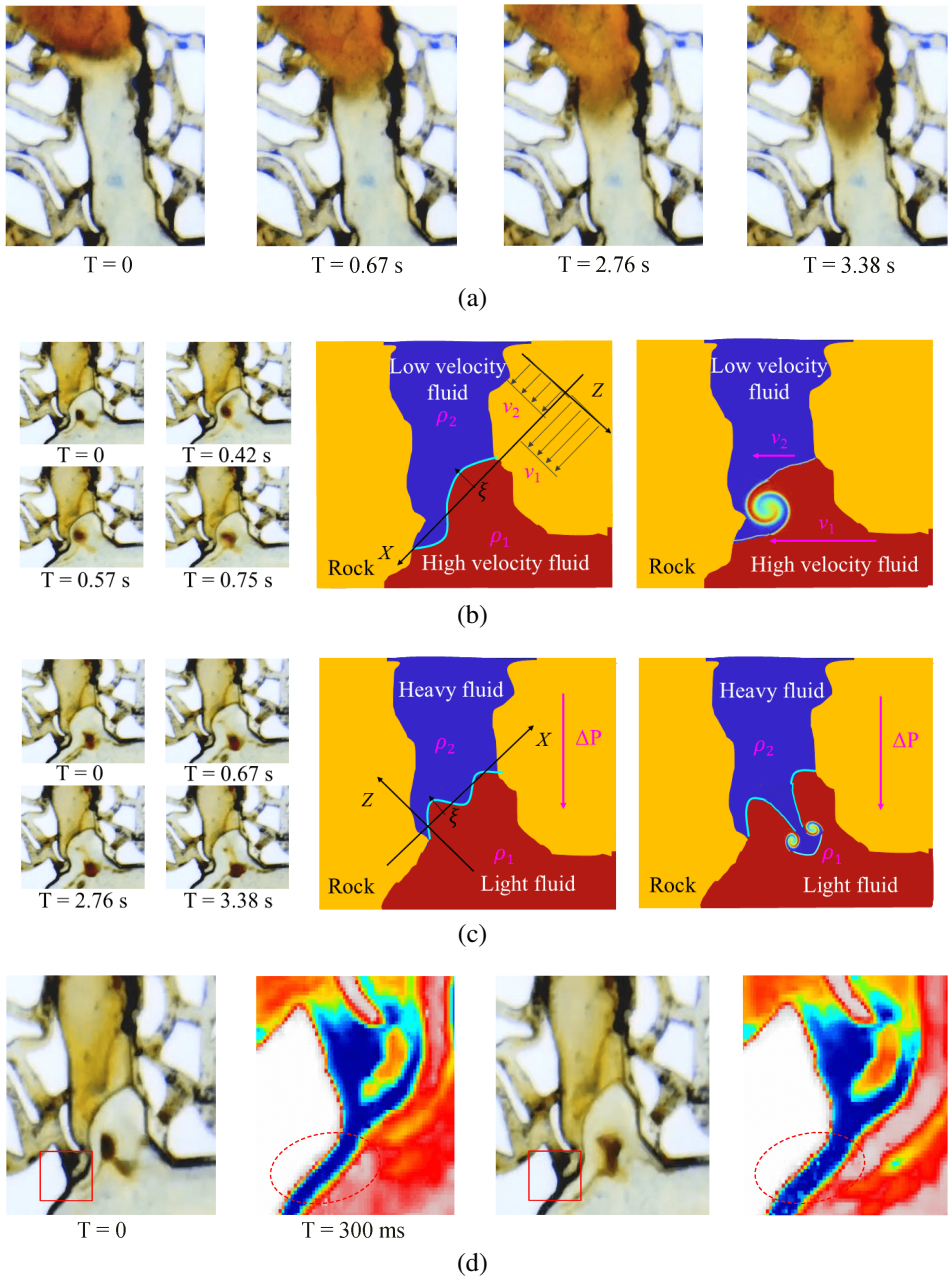

Fig. 10. Uneven mass transfer at interface: (a) Taylor dispersion effect, (b) Kelvin-Helmholtz instability, (c) Rayleigh-Taylor instability, and (d) Marangoni effect.

$$\begin{cases} \left[-\left(U_i+\dfrac{\partial\phi_i}{\partial x}\right)\dfrac{\partial\zeta}{\partial x}+\dfrac{\partial\phi_i}{\partial z}\right]\Bigg|_{z=\xi}=\dfrac{\partial\zeta}{\partial t} \quad (i=1,2) \\ \left(-U_i\dfrac{\partial\zeta}{\partial x}+\dfrac{\partial\phi_i}{\partial z}\right)\Bigg|_{z=0}=\dfrac{\partial\zeta}{\partial t}(i=1,2) \\ \left(\rho_1\dfrac{\partial\phi_1}{\partial t}+\rho_1U_1\dfrac{\partial\phi_1}{\partial x}+\sigma\dfrac{\partial^2\zeta}{\partial x^2}\right)\Bigg|_{z=0}+\rho_1g\eta \\ =\left(\rho_2\dfrac{\partial\phi_2}{\partial t}+\rho_1U_1\dfrac{\partial\phi_1}{\partial x}\right)\Bigg|_{z=0}+\rho_2g\eta \end{cases} \tag{3}$$

where g is the acceleration of gravity, n is the coordinate value when $z=\eta$.

Bringing Eq. (3) into Eq. (1):

$$\begin{aligned} &\frac{\rho_1+\rho_2}{k}\omega^2-2\left(\rho_1U_1+\rho_2U_2\right)\omega+\rho_1kU_1^2+\rho_2kU_2^2 \\ &+\left(\rho_1-\rho_2\right)g-\sigma k^2=0 \\ &\omega=\frac{k\left(\rho_1U_1+\rho_2U_2\right)}{\rho_1+\rho_2} \\ &\pm\frac{k\sqrt{\sigma\left(\rho_1+\rho_2\right)k^2-\rho_1\rho_2\left(U_1-U_2\right)^2-\frac{\rho_1^2-\rho_2^2}{k}g}}{\rho_1+\rho_2} \end{aligned} \tag{4}$$

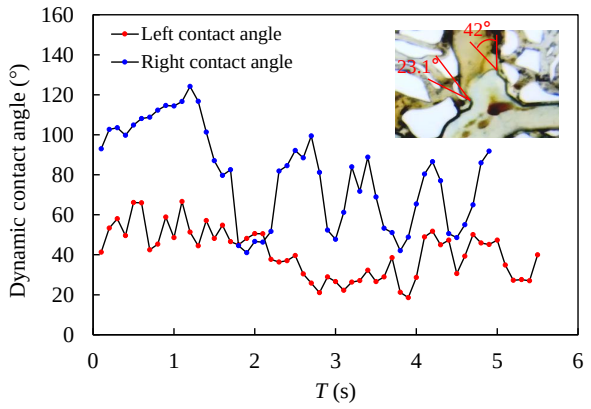

Fig. 11. The curve of dynamic contact angle in the process of interfacial turbulence.

Therefore, the conditions for excitation of interface instability are:

$$\sigma(\rho_1+\rho_2)k^2-\rho_1\rho_2(U_1-U_2)^2-\frac{\rho_1^2-\rho_2^2}{k}g<0 \quad (5)$$

The conditions of K-H instability are related to the density, velocity and interfacial tension of the two phases.

The Rayleigh-Taylor (R-T) instability in CO_2-oil miscible phase (Sharp, 1984; Truzzolillo and Cipelletti, 2017; Lyubimova et al., 2019) is shown in Fig. 10(c). In this experiment, the low-density CO_2 accelerates the high-density oil, and the cylindrical vortex diffusion caused by the density gradient.

It is assumed that the initial velocity of the fluid is 0, and the remaining assumptions are the same as K-H instability. Considering the interfacial tension, the boundary conditions of the model can be obtained as follows:

$$\begin{cases} \left.\dfrac{\partial\phi_1}{\partial x}\right|_{x=+\infty}=0, \quad \left.\dfrac{\partial\phi_2}{\partial x}\right|_{x=-\infty}=0 \\ \left.\left(\dfrac{\partial\phi_i}{\partial z}\right)\right|_{z=0}=\dfrac{\partial\zeta}{\partial t} \quad (i=1,2) \\ \left[\rho_1\dfrac{\partial\phi_1}{\partial t}+\sigma\dfrac{\partial^2\zeta}{\partial x^2}\right]_{z=0}+\rho_1 g\eta=\rho_2\left.\left(\dfrac{\partial\phi_2}{\partial t}\right)\right|_{z=0}+\rho_2 g\eta \end{cases} \quad (6)$$

Bringing Eq. (6) into Eq. (1):

$$\begin{aligned} &\frac{\rho_1\omega^2 a}{k}+\rho_1 ga-\sigma k^2 a=-\frac{\rho_2\omega^2 a}{k}+\rho_2 ga \\ &\omega^2=\frac{k}{\rho_1+\rho_2}\left[\sigma k^2+\left(\rho_2-\rho_1\right)g\right] \end{aligned} \quad (7)$$

Therefore, the interface instability condition is:

$$\frac{k}{\rho_1+\rho_2}\left[\sigma k^2+(\rho_2-\rho_1)g\right]<0 \quad (8)$$

According to Eq. (8), it can be found that the interfacial tension actually plays a stabilizing role. When the interfacial tension exists, even when the density of two fluids $\rho_2<\rho_1$, the fluid may remain stable. R-T instability is only related to density and interfacial tension.

The K-H instability and R-T instability lead to the rapid diffusion of oil in the middle of the two-phase interface, resulting in the concentration difference between the two phases, as shown in Fig. 10(d). This leads to the interfacial tension gradient on the interface, generating a shear force from low interfacial tension to high interfacial tension (middle to both sides of the wall), which induces interfacial instability and oscillation, a phenomenon known as the Marangoni effect (Khosravi et al., 2015; Jia et al., 2020). The interfacial tension is related to temperature and concentration, and only the concentration changes in this experiment.

Before the interface instability occurs, the diffusion rate between CO_2 and oil increases gradually. With the dissolution of CO_2 and the expansion of oil, the light oil component at the two-phase interface increases, so as the contact angle of crude oil. This proves that the quartz wall has different adsorption capacity for different components of crude oil, and the constant change of contact angle is related to the diffusion and composition of the fluid.

The four phenomena in Fig. 10 will cause the interface to fluctuate violently until the components of CO_2 and oil are close to each other, and the interface move to the oil phase end and eventually disappear in the crude oil. The curve of dynamic contact angle in the process of interfacial turbulence is shown in Fig. 11. Due to the influence of CO_2 flow direction, the left contact angle is smaller than the right contact angle. Affected by the Marangoni effect, the change of the left contact angle is relatively stable. The interfacial turbulence leads to the gradient of interfacial tension, which makes the total trend of crude oil contact angle decrease first and then increase, showing a fluctuating form.

Taylor dispersion and Kelvin-Helmholtz instability are key mechanisms promoting CO_2-oil mass transfer. This suggests that in optimizing CO_2 injection schemes for shale reservoirs, increasing the injection rate after entering the supercritical phase can induce interfacial instability, thereby enhancing CO_2-oil miscibility.

3.3 CO_2 huff-n-puff post fracturing

Then, the chip in Section 3.1 was used to perform CO_2 huff-n-puff post fracturing, which helps us to clarify the micro-mechanism of CO_2 huff-n-puff. In addition, the influences of the heterogeneous structure of laminated shale on the occurrence of remaining oil were studied.

3.3.1 The microscopic mechanism of CO_2-oil-water

Without water exist, the main mechanism of miscible CO_2 in the soaking stage is diffusion extraction. When water is present, it both impedes CO_2 from entering the shale matrix pores, creating a water-blocking effect, and blocks some smaller pores, thus increasing the CO_2 sweep area. The mechanism of miscible CO_2 extraction in the presence of water can be divided into direct and indirect methods. Direct extraction is similar to the process without water, while indirect extraction includes dissolution expansion and dissolution extraction. As shown in Fig. 12(a), in dissolution expansion, CO_2 first dissolves in water to form carbonated water, which then enters the oil, causing it to expand. In Fig. 12(b), in dissolution extraction, CO_2 dissolves into water and then

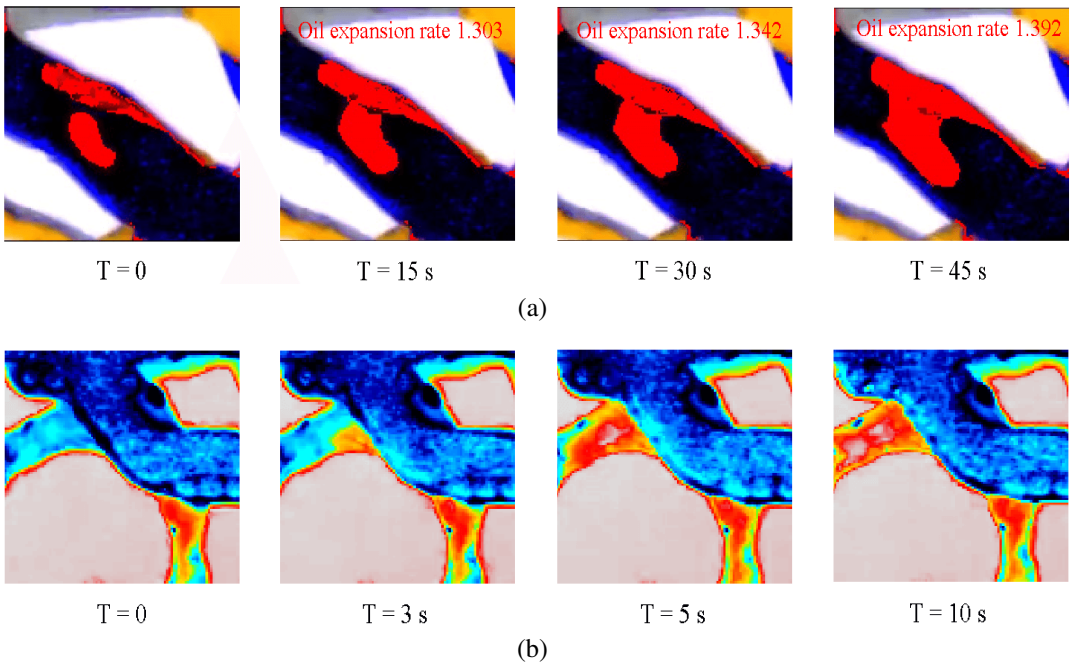

Fig. 12. Microscopic mechanism of CO_2 after fracturing fluid flowback: (a) Dissolution expansion and (b) dissolution extraction.

indirectly extracts the oil. Additionally, when CO_2 dissolves in water, the density of the water increases, enhancing the carrying capacity.

Taylor dispersion and Kelvin-Helmholtz instability are key mechanisms promoting CO_2-oil mass transfer. This suggests that in optimizing CO_2 injection schemes for shale reservoirs, increasing the injection rate after entering the supercritical phase can induce interfacial instability, thereby enhancing CO_2-oil miscibility.

3.3.2 Occurrence of remaining oil and formation reason

The remaining oil distribution figure after water huff-n-puff to the fifth cycle of CO_2 huff-n-puff, and the proportions of different types of remaining oil in different lamina were calculated. For the convenience of analysis, the remaining oil was divided into four types: Cluster, membrane, columnar and isolated drop oil. The residual oil classification method used is consistent with those of Wang et al. (2020) and Li et al. (2021), but we have extended it to laminated shale to study the impact of multiscale heterogeneity on the formation and characteristics of residual oil. In addition, three typical cycles were selected for analysis, which are the end of water huff-n-puff, first and third cycle of CO_2 huff-n-puff. They show the microscopic effects of water, miscible CO_2, and immiscible CO_2 on the occurrence of remaining oil, respectively. The proportion of remaining oil in different layers after each cycle are shown in Fig. 13(a).

The formation of remaining oil is mainly the result of the interaction of six forces (Su et al., 2022; Zhang et al., 2022): viscous shear force τ, viscous force F, separation pressure $\Pi(h)$, pressure gradient (driving force) P, capillary force P_c and adhesion force W. Their calculation formulas are as follows:

$$\begin{cases} \tau = \mu v \\ F = \mu A \dfrac{\mathrm{d}v}{\mathrm{d}x} \\ \Pi(h) = \dfrac{A_H}{6\pi h^3} \\ P = \Delta P \pi r^2 \\ P_c = \dfrac{2\sigma\cos\theta}{r} \\ W = \sigma(1-\cos\theta) \end{cases} \tag{9}$$

where μ is the fluid viscosity, v is the fluid velocity, A is the wall area, ΔP is the pressure difference, σ is the interfacial tension, r is the pore size, θ is the contact angle.

In the water huff-n-puff process, water enters the matrix primarily driven by capillary forces and pressure gradients. Due to the viscosity differences between oil-water and wettability, water is prone to viscous fingering. This causes water to flows along one side of the pore wall, while an oil membrane is formed on the other side as the water file thickens. As shown in Fig. 13(b), the oil membrane is balanced under the action of viscous shear force of water and viscous force between oil and the pore wall, resulting in membrane remaining oil at the end of water huff-n-puff.

Due to the wall water wet, the membrane remaining oil is subjected to a positive separation pressure. According to the formula, when the thickness of the membrane remaining oil is large, it will be separated from the wall under the action of separation pressure. After the oil membrane separates from the pore wall, it reaches equilibrium under the influence of pressure gradient, viscous shear force, and viscous force, forming isolated droplet residual oil. These isolated oil droplets primarily exist in the water flow.

Due to the prevalence of water-wet regions over oil-wet

regions in the chip, membrane and isolated droplet residual oils are more common after the water huff-n-puff process, while columnar residual oil is less prevalent. Additionally, the significant viscosity difference between oil and water leads to viscous fingering, causing water to break through and form preferential flow channels, preventing further expansion of the water-swept area. Water has a poor carrying capacity for oil in the swept regions, resulting in low recovery rates. As shown in Fig. 13(a), water primarily affects limestone layer 1, while the swept areas in the other three layers are minimal and displacement is incomplete, resulting in a significant amount of clustered residual oil. In the mudstone layers, the presence of oil-wet regions provides greater resistance to water entry, leading to a relatively higher content of clustered residual oil in the two mudstone laminas.

In the first CO_2 huff-n-puff cycle, the viscosity and density difference between oil and CO_2 decreases under miscible conditions, effectively reducing viscous fingering. In addition, the water resistance effect impedes CO_2 entry to larger pores, forcing CO_2 into smaller oil-filled pores, thereby increasing the swept area. At the same time, water also enhances mobility after dissolving CO_2 and improves oil recovery. During the depressurization process, CO_2 becomes immiscible as pressure drops. Due to the differences in viscosity and wettability, CO_2 moves quickly through the center part of the pores, which helps breaks cluster remaining oil, thereby improving EOR. The gray value analysis of miscible CO_2 and immiscible CO_2 is shown in Fig. 13(c). Miscible CO_2-oil shows no clear interface, while immiscible CO-oil has a distinct interface, affecting the mass transfer rate between CO_2 and oil. Therefore, miscible and immiscible CO_2 exhibit different mechanisms for oil recovery.

As shown in Fig. 13(a), after the first cycle of CO_2 huff-n-puff, the remaining oil in layer 1 is reduced by 8.93% compared with that after water huff-n-puff. The remaining oil in layer 2 increased by 2.86% compared with that after water huff-n-puff. After the third cycle of CO_2 huff-n-puff, the remaining oil in layer 2 decreased by 9.08% compared with that after water huff-n-puff. This indicates that the miscible CO_2 enters the matrix by diffusion, which will cause a small amount of cluster remaining oil in the oil-wet zone of the mudstone layer 1 to migrate to deeper layer 2, as shown in the right picture in Fig. 13(a).

The immiscible CO_2 has a displacement-carry effect on the cluster remaining oil. In the second cycle of CO_2 huff-n-puff, this part of the cluster remaining oil is migrated to layer 1, as shown in the right picture in Fig. 13(a). As shown in the left side of Fig. 13(d), after the second cycle of CO_2 huff-n-puff, the cluster remaining oil in the oil-wet area is dispersed to form a large number of columnar remaining oil under the action of pressure gradient, capillary force and viscous force. As shown on the right side of Fig. 13(d), a small amount of oil forms membrane remaining oil under the action of viscous shear force and adhesion force. And as the number of huff-n-puff increases, the cluster remaining oil continues to transform into columnar remaining oil and is migrated downward the chip. When this part of the remaining oil flows through the mudstone oil-wet zone, it will stay under the action of capillary resistance. Therefore, with the increase of CO_2 huff-n-puff cycle number, the content of columnar remaining oil increases continuously, and it is mainly distributed in the mudstone oil wet area.

Due to the extraction of CO_2 on crude oil, isolated droplet residual oil is mostly found within the water phase. Columnar residual oil is primarily located in CO_2-containing oil-wet pores and its quantity increases with the number of huff-n-puff cycles. Membrane residual oil predominantly coexists with water, with a smaller amount present in CO_2. In limestone layer 1, which has a higher water content, membrane residual oil is mainly distributed. However, as limestone layer 1 is the primary area affected by CO_2, the majority of the membrane residual oil is extracted with increasing huff-n-puff cycles. The formation of membrane residual oil in water huff-n-puff is due to wettability effects, while in CO_2, it is caused by the precipitation of dissolved gas and the adsorption of heavy crude oil.

Overall, from the end of water huff-n-puff to the end of the third cycle of CO_2 huff-n-puff, the content of isolated droplet remaining oil decreased by 1.23%, accounting for 89.78% of the total isolated droplet remaining oil after water huff-n-puff. The content of columnar remaining oil increased by 1.78%, making up 31.85% of the total columnar remaining oil present during water huff-n-puff. The content of membrane remaining oil decreased by 2.98%, representing 47.23% of the total membrane remaining oil after water huff-n-puff. The content of cluster remaining oil decreased by 16.06%, which is 69.89% of the total cluster remaining oil present after water huff-n-puff. The displacement-carry effect of immiscible CO_2 is a key mechanism for extracting large amounts of clustered residual oil. When the pressure drops below the supercritical pressure of CO_2, its volume rapidly expands, releasing significant elastic energy.

4. Conclusions

This study considers factors such as multiscale heterogeneous pore-fracture structures, heterogeneous wettability, and pressure in shale, simulating the post-fracturing fluid flowback and CO_2 huff-n-puff process in a laminated shale matrix-fracture microfluidic chip. Specific results are as follows:

1) Forced imbibition is the primary mechanism of fracturing fluid, affecting the water-wet macropores in both limestone and mudstone layers, while spontaneous imbibition impacts smaller pores such as clay minerals in mudstone. In the first cycle, the ratio of forced to spontaneous imbibition is 89.3% to 10.7%.
2) Pressure and pore structure are the main factors influencing the solubility and diffusion rate of CO_2, resulting in different oil recovery mechanisms at various stages. Low-pressure CO_2 exhibits displacement-carry effects, supercritical CO_2 shows dissolution and extraction, and miscible CO_2 demonstrates diffusion and extraction.
3) Differences in pressure, velocity, density, and interfacial tension cause Taylor dispersion, Kelvin-Helmholtz instability, Rayleigh-Taylor instability, and the Marangoni effect, leading to interfacial turbulence, accelerating CO_2-

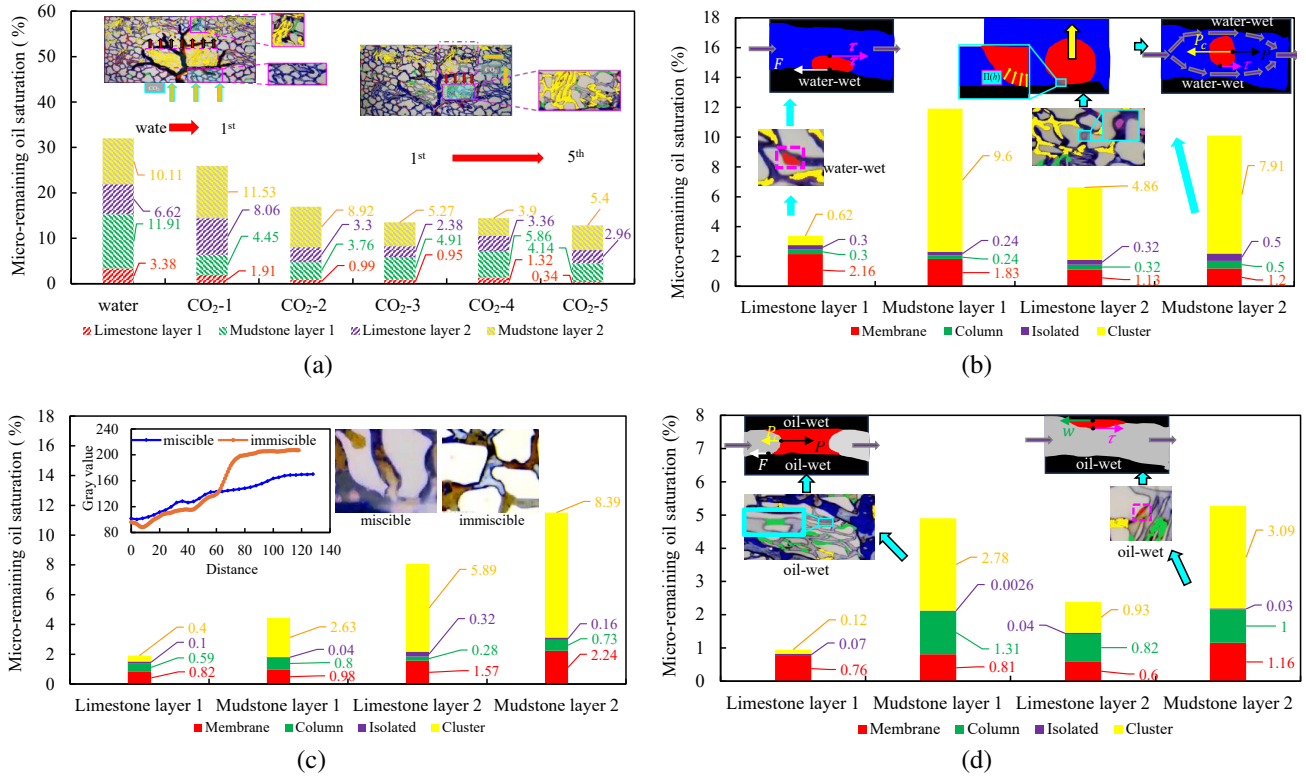

Fig. 13. The proportion of micro-remaining oil in different layers: (a) After each cycle, (b) at the end of water huff-n-puff, (c) at the end of 1st CO_2 huff-n-puff cycle, and (d) at the end of 3rd CO_2 huff-n-puff cycle.

oil miscibility.

4) After fracturing fluid backflow, residual oil forms as films, isolated droplets, and clusters. Miscible CO_2 can penetrate dead oil zones and enhance oil recovery through diffusion and extraction, while immiscible CO_2 disrupts clustered residual oil and extracts oil through elastic energy.

In future research, we will explore the long-term stability of CO_2 sequestration in reservoirs and investigate additional development methods, such as injecting fracturing fluid after pre-injecting CO_2. We aim to extend the findings from microfluidic experiments to the feasibility of field-scale operations, providing optimized solutions.

Acknowledgements

This work was supported by the Fundamental Research Funds for the Central Universities (No. 24CX02015A), the National Natural Science Foundation of China (No. 52374064), the Fund of State Key Laboratory of Deep Oil and Gas (No. SKLDOG2024-ZYTS-14), and the financial support from the Shandong Provincial Universities Youth Innovation and Technology Support Program (No. 2022KJ065). The authors also appreciate the technical support by Maolei Cui and Jun Niu from Sinopec Petroleum Exploration and Production Research Institute.

Conflict of interest

The authors declare no competing interest.

References

Bachu, S. Identification of oil reservoirs suitable for CO_2-EOR and CO_2 storage (CCUS) using reserves databases, with application to Alberta, Canada. International Journal of Greenhouse Gas Control, 2016, 44: 152-165.

Cai, J., Jiao, X., Wang, H., et al. Multiphase fluid-rock interactions and flow behaviors in shale nanopores: A comprehensive review. Earth-Science Reviews, 2024, 257: 104884.

Cai, J., Yu, B. A discussion of the effect of tortuosity on the capillary imbibition in porous media. Transport in Porous Media, 2011, 89(2): 251-263.

Chen, H., Li, B., Duncan, I., et al. Empirical correlations for prediction of minimum miscible pressure and near-miscible pressure interval for oil and CO_2 systems. Fuel, 2020, 278: 118272.

Chen, X., Yu, H., Cao, A., et al. Study on enhanced oil recovery mechanism of CO_2 miscible flooding in heterogeneous reservoirs under different injection methods. ACS Omega, 2023, 8(27): 24663-24672.

Conn, C. A., Ma, K., Hirasaki, G. J., et al. Visualizing oil displacement with foam in a microfluidic device with permeability contrast. Lab on a Chip, 2014, 14(20): 3968-3977.

Deng, L., King, M. J. Theoretical investigation of the transition from spontaneous to forced imbibition. SPE Journal, 2019, 24(1): 215-229.

Fang, Y., Zhang, W., Ma, F., et al. Research on the global distribution and development status of shale oil. Conservation and Utilization of Mineral Resources, 2019, 39(5): 126-134.

Fani, M., Pourafshary, P., Mostaghimi, P., et al. Application of microfluidics in chemical enhanced oil recovery: A review. Fuel, 2022, 315: 123225.

Feng, Q., Xu, S., Xing, X., et al. Advances and challenges in shale oil development: A critical review. Advances in Geo-Energy Research, 2020, 4(4): 406-418.

Frankel, I., Brenner, H. On the foundations of generalized Taylor dispersion theory. Journal of Fluid Mechanics, 1989, 204: 97-119.

Funada, T., Joseph, D. Viscous potential flow analysis of Kelvin-Helmholtz instability in a channel. Journal of Fluid Mechanics, 2001, 445: 263-283.

Gao, Y., Li, Q., He, X., et al. Quantitative evaluation of shale-oil recovery during CO_2 huff-n-puff at different pore scales. Energy & Fuels, 2021, 35(20): 16607-16616.

Gong, X., Gonzalez, R., McVay, D. A., et al. Bayesian probabilistic decline-curve analysis reliably quantifies uncertainty in shale-well-production forecasts. SPE Journal, 2014, 19(6): 1047-1057.

Hu, S., Zhao, W., Hou, L., et al. Development potential and technical strategy of continental shale oil in China. Petroleum Exploration and Development, 2020, 47(4): 877-887.

Jia, F., Sun, K., Zhang, P., et al. Marangoni effect on the impact of droplets onto a liquid-gas interface. Physical Review Fluids, 2020, 5(7): 073605.

Jian, G., Gizzatov, A., Kawelah, M., et al. Simply built microfluidics for fast screening of CO_2 foam surfactants and foam model parameters estimation. Applied Energy, 2021, 292: 116815.

Khosravi, M., Rostami, B., Emadi, M., et al. Marangoni flow: An unknown mechanism for oil recovery during near-miscible CO_2 injection. Journal of Petroleum Science and Engineering, 2015, 125: 263-268.

Lifton, V. A. Microfluidics: An enabling screening technology for enhanced oil recovery (EOR). Lab on a Chip, 2016, 16(10): 1777-1796.

Li, L., Su, Y., Hao, Y., et al. A comparative study of CO_2 and N_2 huff-n-puff EOR performance in shale oil production. Journal of Petroleum Science and Engineering, 2019a, 181: 106174.

Li, L., Su, Y., Sheng, J. J., et al. Experimental and numerical study on CO_2 sweep volume during CO_2 huff-n-puff enhanced oil recovery process in shale oil reservoirs. Energy & Fuels, 2019b, 33(5): 4017-4032.

Liu, F., Wang, X., Yang, H., et al. Miscibility characteristics of CO_2-Oil in tight sandstone reservoirs: Insights from molecular dynamics simulations. ACS Omega, 2024, 9(13): 15663-15676.

Li, Y., Zhang, J., Pan, D., et al. Occurrence laws of microscopic remaining oil in high water-cut reservoirs: A case study on blocks Xiaoji and Gangxi in Dagang Oilfield. Xinjiang Petroleum Geology, 2021, 42(4): 444-449. (in Chinese)

Lyubimova, T., Vorobev, A., Prokopev, S. Rayleigh-Taylor instability of a miscible interface in a confined domain. Physics of Fluids, 2019, 31(1): 014104.

Mahdavifar, M., Roozshenas, A. A., Miri, R. Microfluidic experiments and numerical modeling of pore-scale asphaltene deposition: Insights and predictive capabilities. Energy, 2023, 283: 129210.

Mohagheghian, E., Hassanzadeh, H., Chen, Z. CO_2 sequestration coupled with enhanced gas recovery in shale gas reservoirs. Journal of CO_2 Utilization, 2019, 34: 646-655.

Nguyen, P., Carey, J. W., Viswanathan, H. S., et al. Effectiveness of supercritical-CO_2 and N_2 huff-and-puff methods of enhanced oil recovery in shale fracture networks using microfluidic experiments. Applied Energy, 2018, 230: 160-174.

Ren, B., Male, F., Duncan, I. J. Economic analysis of CCUS: Accelerated development for CO_2 EOR and storage in residual oil zones under the context of 45Q tax credit. Applied Energy, 2022, 321: 119393.

Salles, J., Thovert, J. F., Delannay, R., et al. Taylor dispersion in porous media. Determination of the dispersion tensor. Physics of Fluids A: Fluid Dynamics, 1993, 5(10): 2348-2376.

Sang, Q., Zhao, X., Liu, Y., et al. Effects of the laminated-structure and mixed wettability on the oil/water relative permeabilities and oil productions in shale oil formations. Journal of Petroleum Science and Engineering, 2022, 208: 109457.

Sharp, D. H. An overview of Rayleigh-Taylor instability. Physica D: Nonlinear Phenomena, 1984, 12(1-3): 3-18.

Sieben, V. J., Tharanivasan, A. K., Ratulowski, J., et al. Asphaltenes yield curve measurements on a microfluidic platform. Lab on a Chip, 2015, 15(20): 4062-4074.

Su, Y., Zhang, X., Li, L., et al. Experimental study on microscopic mechanisms and displacement efficiency of N_2 flooding in deep-buried clastic reservoirs. Journal of Petroleum Science and Engineering, 2022, 208: 109789.

Tan, P., Jin, Y., Han, K., et al. Analysis of hydraulic fracture initiation and vertical propagation behavior in laminated shale formation. Fuel, 2017, 206: 482-493.

Truzzolillo, D., Cipelletti, L. Hydrodynamic instabilities in miscible fluids. Journal of Physics: Condensed Matter, 2017, 30(3): 033001.

Wang, C., Jiang, H., Ma, M., et al. Study of the variation of pore-scale residual oil flow based on a microfluidic model. Petroleum Science Bulletin, 2020, 5(3): 376-391. (in Chinese)

Wang, H., Cai, J., Su, Y., Jin, Z., et al. Imbibition behaviors in shale nanoporous media from pore-scale perspectives. Capillarity, 2023, 9(2): 32-44.

Wang, K., You, Q., Long, Q. M., et al. Experimental study of the mechanism of nanofluid in enhancing the oil recovery in low permeability reservoirs using microfluidics. Petroleum Science, 2023, 20(1): 382-395.

Wang, T., Tian, S., Li, G., et al. Molecular simulation of

CO_2/CH_4 competitive adsorption on shale kerogen for CO_2 sequestration and enhanced gas recovery. The Journal of Physical Chemistry C, 2018, 122(30): 17009-17018.

Wang, X., Zhang, G., Tang, W., et al. A review of commercial development of continental shale oil in China. Energy Geoscience, 2022, 3(3): 282-289.

Yang, Y., Song, H., Li, Y., et al. Microscopic mechanism of CO_2 huff-n-puff promoting shale oil mobilization in nanopores. Fuel, 2024, 371: 131841.

Zeng, T., Miller, C. S., Mohanty, K. K. Combination of a chemical blend with CO_2 huff-n-puff for enhanced oil recovery in oil shales. Journal of Petroleum Science and Engineering, 2020, 194: 107546.

Zhang, S., Liu, H., Liu, Y., et al. Main controls and geological sweet spot types in Paleogene shale oil rich areas of the Jiyang Depression, Bohai Bay basin, China. Marine and Petroleum Geology, 2020, 111: 576-587.

Zhang, X., Li, L., Su, Y., et al. Microfluidic investigation on multiphase interaction and flow behavior of immiscible/miscible gases in deep heterogeneous reservoir. Journal of Environmental Chemical Engineering, 2022, 10(6): 109036.

Zhang, X., Li, L., Su, Y., et al. Microfluidic investigation on asphaltene interfaces attempts to carbon sequestration and leakage: Oil-CO_2 phase interaction characteristics at ultrahigh temperature and pressure. Applied Energy, 2023, 348: 121518.

Zhang, Z., Pan, S., Li, H., et al. Recent advances in carbon dioxide utilization. Renewable and Sustainable Energy Reviews, 2020, 125: 109799.

Zhao, J., Wang, L., Liu, S., et al. Numerical simulation and thermo-hydro-mechanical coupling model of in situ mining of low-mature organic-rich shale by convection heating. Advances in Geo-Energy Research, 2022, 6(6): 502-514.